Particles II

Access the latest eBook →

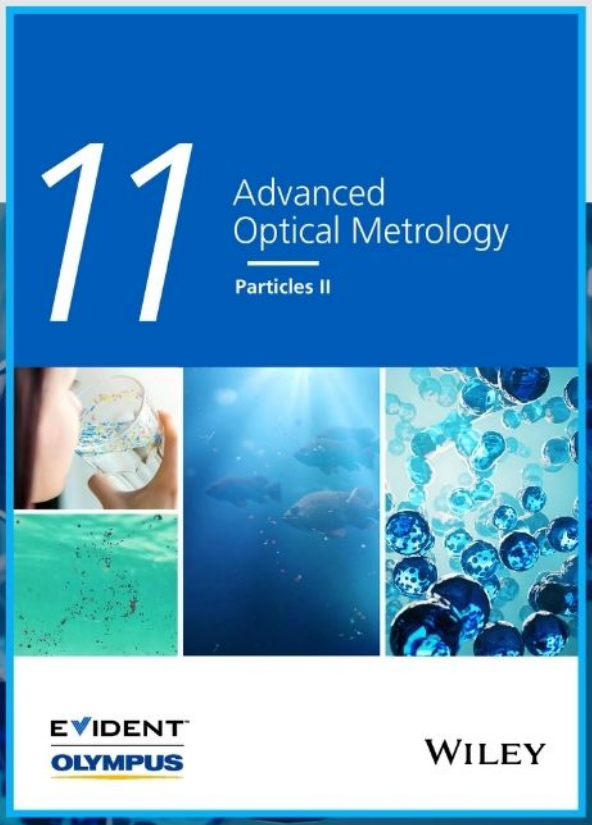

Impact on Biological Systems and the Environment

This eBook is dedicated to the research of Professor David Wertheim.
In collaboration with various groups, Professor Wertheim uses confocal microscopy to analyse the impact of different types of particles on human health and the environment, with a focus on human health-hazardous particles detected with solid-state nuclear track detectors (SSNTD). Download for free, today.

EVIDENT
OLYMPUS

WILEY

ADVANCED MATERIALS
www.advmat.de

Cluster-Glass for Low-Cost White-Light Emission

*Irán Rojas-León, Jan Christmann, Sebastian Schwan, Ferdinand Ziese, Simone Sanna, Doreen Mollenhauer, Nils W. Rosemann, and Stefanie Dehnen**

The development of efficient and high-brilliance white-light sources is an essential contribution to innovative emission technologies. Materials exhibiting strong nonlinear optical properties, in particular second-harmonic generation (SHG) or white-light generation (WLG), have therefore been investigated with great activity in recent times. While many new approaches have been reported until now, the processability of the compounds remains a challenge. Here, a new class of materials, denoted as "cluster-glass", which do not only show superior white-light emission properties upon irradiation by an inexpensive continuous-wave infrared laser diode, but can be easily accommodated in size and shape by formation of robust glassy solids, is introduced. The cluster-glass materials are fabricated by mild heating from crystalline powders of adamantane-type clusters exhibiting a quaternary, inorganic–organic hybrid cluster core $[(PhSi)(CH_2)_3(PhSn)E_3]$ (E = S, Se, Te). The process is fully reversible and preserves the integrity of the clusters in the glass, as proven by solution spectroscopy and recrystallization. Theoretical studies corroborate the importance of the quaternary nature of the cluster cores for the observed structural and optical phenomena. Thanks to these findings, high-brilliance white-light sources can be synthesized in form of stable, robust glass of any shape, which ultimately renders them suitable for everyday's applications.

1. Introduction

Materials exhibiting nonlinear optical properties by frequency doubling (second-harmonic generation, SHG) or supercontinuum generation (white-light generation, WLG) have been in the focus of the scientific community for a long time.[1–13] The term "supercontinuum generation" describes an extreme spectral broadening of an originally monochromatic light beam upon propagating through a nonlinear medium,[8,10] as an alternative to the conventional generation of white light by means of inorganic phosphors or inorganic as well as organic semiconductors.[14–16] The broad spectrum obtained may cover the entire visible spectral range; in these cases, the observed emission resembles white light and the process is therefore referred to as WLG. The physical mechanisms underlying supercontinuum generation can be diverse—and can also occur as a combination of nonlinear optical effects, like self-phase and cross-phase modulation, four-wave mixing, or solitonic phenomena.[17–20] While in most cases pulsed-laser sources are required for such processes, WLG upon irradiation of a material with a near-infrared continuous-wave (NIR CW) laser of significantly lower costs (by a factor of $\approx 10^3 \ldots 10^4$ as compared to the pulsed lasers) has been reported for (doped) oxides or oxidic hybrid compounds, for complexes of rare-earth metals, and for carbon-based solids.[1] Given the complexity of the processes, different compounds exhibiting WLG can show the extreme nonlinear effects owing to different reasons or different combinations of mechanisms, which in many cases have not yet been fully elucidated to date.

I. Rojas-León, J. Christmann, S. Dehnen
Department of Chemistry
Philipps University Marburg
DE-35032 Marburg, Germany
E-mail: dehnen@chemie.uni-marburg.de

I. Rojas-León, J. Christmann, S. Dehnen
Scientific Center of Materials Science
Philipps University Marburg
DE-35032 Marburg, Germany

The ORCID identification number(s) for the author(s) of this article can be found under https://doi.org/10.1002/adma.202203351.

DOI: 10.1002/adma.202203351

S. Schwan, D. Mollenhauer
Institute of Physical Chemistry
Justus-Liebig University Giessen
DE-35392 Giessen, Germany

S. Schwan, F. Ziese, S. Sanna, D. Mollenhauer
Center for Materials Research (ZfM)
Justus-Liebig University Giessen
DE-35392 Giessen, Germany

F. Ziese, S. Sanna
Institute for Theoretical Physics
Justus-Liebig University Giessen
DE-35392 Giessen, Germany

N. W. Rosemann
Light Technology Institute
Karlsruhe Institute of Technology
DE-76131 Karlsruhe, Germany

The last years have witnessed a highly increased interest in this field, which is mainly due to applications in everyday devices.[3–7] Recently, a class of amorphous molecular materials have been shown to convert infrared light of a low-cost CW laser diode into highly directional white light with surprising brilliance.[2] These materials comprise organic adamantane derivatives or inorganic adamantane-type compounds that share the general formula $[(RT)_4E_6]$, in which R is an organic substituent, T represents a group 14 atom (C, Si, Ge, Sn), and E represents a chalcogenide atom (S, Se, Te) or CH_2. During variation of the components R, T, and E, it was confirmed that the extremely low degree of periodical order of the molecules in the amorphous powders seems to be one of the necessary preconditions for WLG.[21–24] A second one is the nature of the organic substituents R: these need to be aromatic or other cyclic substituents that possess a high electron density, like styryl, phenyl, η^1-cyclopentadienyl, cyclohexyl, or $CH_2CH_2(C_6H_4)CO_2Et$. In contrast, crystalline or sufficiently ordered samples, such as $[(PhSi)_4S_6]$, $[(NpSi)_4S_6]$, and $[(NpSn)_4S_6]$, and samples that are equipped with aliphatic chains such as $[(MeSn)_4S_6]$ or $[(BuSn)_4S_6]$, do not show WLG, but exhibit intense SHG instead.[25,26]

A major drawback of the powders investigated so far, however, is their poor processability owing to either high melting points or decomposition prior to melting on the one hand, or sensitivity to air on the other hand, or both. We therefore aimed at the development of new types of amorphous molecular solids, which do not only fulfill the described requirements, but in addition show the materials properties necessary for technical application.

Here, we present our strategy to reach this goal by the formation of hybrid adamantane-type clusters of the type $[(RT^1)(CH_2)_3(RT^2)E_3]$, based on quaternary adamantane-type cages $\{T^1(CH_2)_3T^2E_3\}$ with two different group 14 atoms, T^1 and T^2, and two types of bridging units, CH_2 and E. These combine inorganic and organic parts in one molecule, which serves to combine the high air stability of the first with the lower melting point of the second. The approach allowed for a smooth and reversible transformation of the as-prepared powders into a so far unprecedented class of materials that we denominate as "cluster-glass". We studied the transformation processes that includes a transition from crystallinity to perfect amorphousness of the compounds, with the latter exhibiting superior WLG properties upon irradiation with infrared laser light. Optical spectroscopy indicated that, while the crystalline materials do not show 2nd order nonlinear optical properties owing to their centrosymmetric structures, the cluster-glass materials are capable of WLG. The interaction between the cluster molecules in the materials and their optical response was studied in detail by means of quantum chemical computations.

2. Synthesis and Crystal Structures of Adamantane-Type Clusters Based on Quaternary Cluster Cores

Novel compounds comprising adamantane-type cluster according to the general formula $[RSi(CH_2SnPh)_3E_3]$, with two different types of group 14 atoms (T^1 = Si, T^2 = Sn) and two different types of bridging groups/atoms (CH_2 and E = S, Se, or Te) were formed using a tetranuclear organo-group 14 tecton, $C_6H_5Si(CH_2PhSnCl_2)_3$ = $PhSi(CH_2PhSnCl_2)_3$, which was generated following a recent report.[27] The reaction sequence employed for the synthesis of the tecton and the subsequent formation of adamantane-type clusters $[PhSi(CH_2SnPh)_3E_3]$ (**1–3**; E = S, Se, Te) is illustrated in **Figure 1**a.

The procedure enabled access of $PhSi(CH_2PhSnCl_2)_3$ in yields on the gram scale. Compounds **1–3** were synthesized from this tecton by addition of TMS_2E (E = S, Se, and Te) in toluene. Upon evaporation of the solvent in vacuo, the raw solid was washed with hexane and isolated in pure form by filtration. $PhSi(CH_2PhSnCl_2)_3$ and **1–3** were fully characterized by elemental analysis, electrospray-ionization mass spectrometry, ^{1}H, ^{13}C, ^{29}Si, ^{77}Se, ^{125}Te, and ^{119}Sn NMR spectroscopy including correlatated spectroscopy (COSY), heteronuclear single quantum coherence (HSQC), and heteronuclear single quantum coherence studies, as well as vibrational spectroscopy (Figures S1–S36, Supporting Information). All compounds were obtained in good yields (55–65%) and all spectroscopic data are in agreement with data reported for related compounds.[28–35] It is worth noting that **1–3** represent rare examples of heteroadamantane-type cores with more than two components, and **3** adds to the very few adamantane-type compounds comprising telluride ligands in the cluster core, with the only known examples of this type so far being $[\{Cp(CO)_3Mo\}_4Sn_4Te_6]$, $[Si_4(CH_2)_2Te_4Me_4]$, and $[Si_4Te_6\{N(SiMe_3)Dipp\}_4]$.[28,29,36] Regarding compound **3**, we emphasize in addition that our synthesis protocol affords a single product of a tellurium-based adamantane cluster with high purity according to ^{125}Te-NMR spectroscopy—in striking contrast to the (few) reported methods to form related compounds, which always yielded mixtures with other species.[28,29]

Single crystals of all the compounds, **1–3**, were obtained from a hexane solution. They were suitable for single-crystal X-ray diffraction (SC-XRD, Table S1, Supporting Information), which served to verify their compositions and to elucidate the molecular and crystal structures. However, we noticed a varying tendency to form single-crystals along this homologous series, which is in line with the observation that some organo-group 14 chalcogenide clusters with adamantane-type shape do inherently not crystallize at all, depending on the combination of R, T, and E.

Compound **1** crystallizes in the triclinic crystal system (space group type $P\bar{1}$), **2** and **3** crystallize in the monoclinic crystal system (space group type $P2_1/c$). The molecular structures of **1–3** are shown in Figure 1b–d, selected structural parameters are listed in Table S2 (Supporting Information). While the cluster molecules in **1** and **2** form dimers via C—H$\cdots\pi$ or T-shape $\pi\cdots\pi$ interactions between four of the phenyl groups, secondary Te$\cdots$Te interactions involving two of the three tellurium atoms per cluster molecules lead to an assembly into zig–zag chains extending along the crystallographic *c* axis in compound **3**.

Three Sn and three chalcogen atoms (E = S, Se, or Te) form a six-membered ring in chair conformation. The six membered ring builds the base of the adamantane like core, on which the $\{RSi(CH_2)_3\}$ entity is sitting like a tapered roof. In contrast to

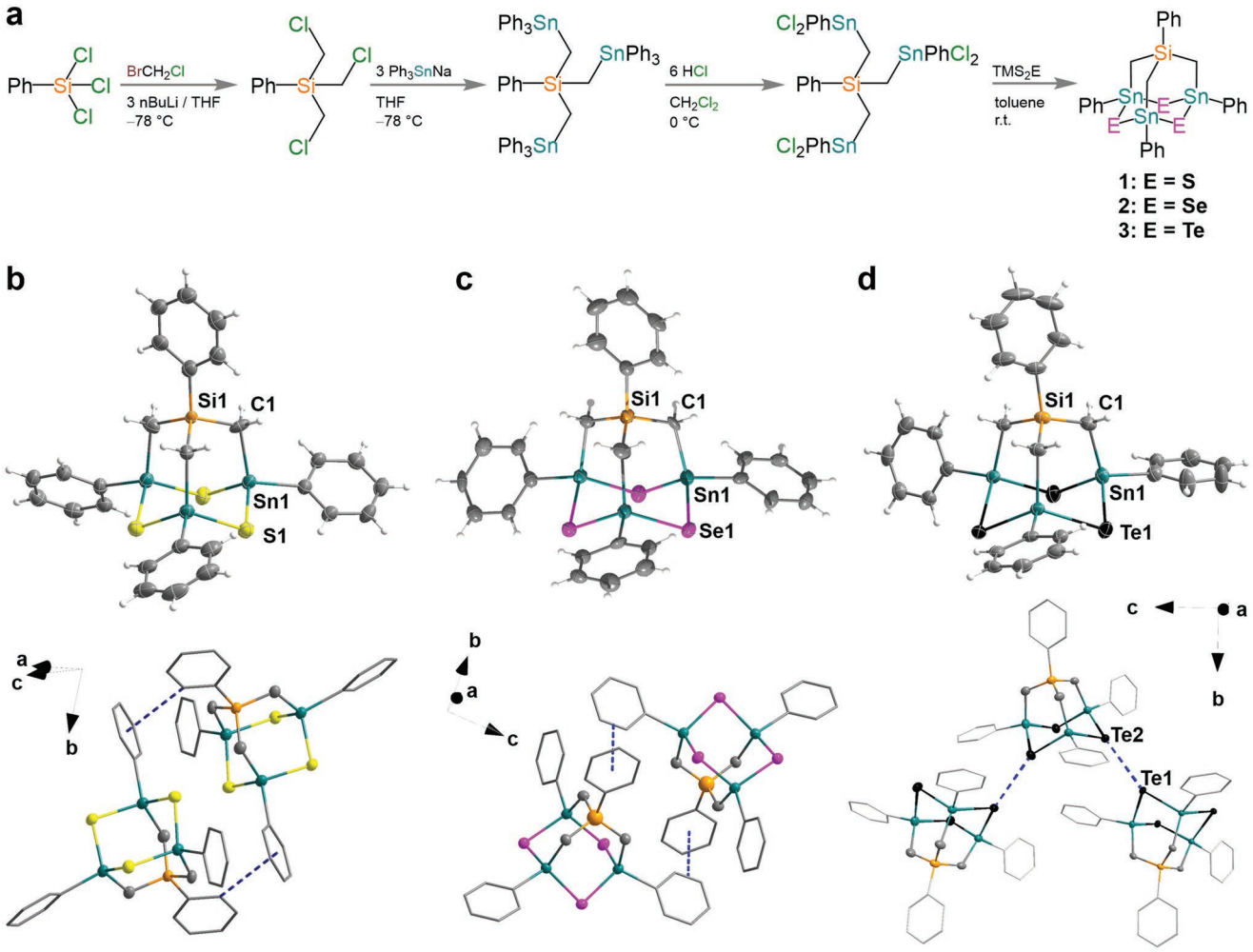

Figure 1. Synthesis and crystal structures of cluster compounds based on quaternary adamantane-type cluster cores. a) Reaction scheme for the synthesis of compounds **1**–**3**. b) Molecular structure of one of the two independent molecules in compound 1 (top) and the inversion-symmetric dimer yielding from C—H···π interactions between phenyl groups (bottom). c) Molecular structure of compound **2** (top) and the inversion-symmetric dimer yielding from T-shaped π···π interactions between phenyl groups (bottom). d) Molecular structure of compound **3** (top) and secondary Te···Te contacts leading to zig–zag chains of clusters extending along the crystallographic *c* axis (bottom). Closest distances between the phenyl rings (**1**, **2**) or the tellurium atoms (**3**) of neighboring cluster molecules are indicated by dashed lines. Hydrogen atoms not involved in intra- or intermolecular hydrogen bonding are omitted for clarity. Thermal ellipsoids are drawn at the 50% probability level.

the regular binary adamantane-type cluster cores of (perfect or idealized) T_d symmetry, the quaternary cores in the title compounds are heavily distorted: while a binary $\{Sn_4E_6\}$ unit comprises 12 identical Sn—E bonds, the quaternary variant comprises three different types of interatomic interactions: six Sn—E bonds, three Sn—C bonds, and three Si—C bonds. The difference between the corresponding interatomic distances—and thus the irregularity of the cluster cores, get more significant with increasing atomic size of the respective chalcogen atom E (a detailed discussion of the structural features of **1**, **2**, and **3** can be found in Note S1, Supporting Information).[29,36–40] This molecular inhomogeneity is the bases for the materials behavior, as reported and discussed in Sections 3–6. Note that related compounds of the type $[(R^1T^1)(CH_2)_3(R^2T^2)E_3]$ were recently reported for R^1 = Me, and E = O), which we modified here to be electron-rich substituents Ph for R^1 and R^2 besides more electron-rich chalcogen ligands E = S, Se, and Te.[40]

3. Cluster-Glass Formation from Crystals of Quaternary Adamantane-Type Cluster Compounds

As compounds **1**–**3** are crystalline, and crystallize in centrosymmetric space groups, they do not exhibit 2nd order nonlinear optical properties per se. This was proven both for samples crystallized by means of slow diffusion-layering and for samples isolated upon rapid solvent evaporation and is summarized below. However, the hybrid nature of the clusters prompted us to study their melting behavior, which indicated that they do not only melt at moderate temperatures, but also form a perfectly amorphous glass without losing their molecular identity. This was demonstrated in a cyclic process, which is schematically illustrated in **Figure 2**.

Monitoring of the persisting identity of the compounds while significantly changing their materials properties is documented in **Figure 3** for compound **2**, as an example for all three

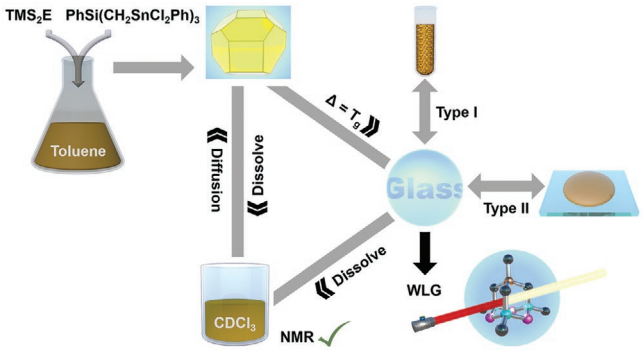

Figure 2. Schematic illustration of the glass formation processes from crystalline powders of hybrid adamantane-type clusters. The initial formation of compounds **1**–**3** as single crystals (left) is followed by thermal treatment to form the glass (right); these were obtained in two types, either by melting within a capillary (type I) or on a flat surface (type II) and exhibit nonlinear optical properties (bottom right). As both the crystals and the glass dissolve readily in $CDCl_3$ it was proven by NMR spectroscopy that they are identical; moreover, the crystalline powder can be recovered from these solutions in a fully reversible manner to close the cycle of this process.

compounds, which show a very similar behavior (for corresponding information for compounds **1** and **3**, see Figures S37 and S39, Supporting Information). The transfer from crystalline powders to cluster-glass materials based on quaternary adamantane-type cages was realized in one of two ways. The first one made use of the melt-quenching technique in melting point determination tubes (80 × 1.3 mm), filled with 5 mg of the compounds as crystalline powders. Starting out from the crystalline samples according to powder X-ray diffraction (PXRD, Figure 3a), the systems were left under vacuum for 30 min and the capillaries sealed thereupon. Then, the solids were heated in a melting point meter with a temperature ramp of 1 °C s^{-1} (Video S1, Supporting Information). As soon as the samples reached the transition temperature (T_g) and the phase change was observed, the capillaries were removed and cooled to room temperature. PXRD studies confirmed the resulting cluster-glass to be highly amorphous (Figure 3b). ^{1}H NMR experiments were carried out before and after glass-formation of the adamantane-clusters, which confirmed that the adamantane-type clusters did not decompose during the glass-transition (Figure 3c). Furthermore, preservation of the compound was proven by energy-dispersive X-ray (EDX) analyses (Figure 3d). To study the glass-transition into more detail, thermogravimetric analysis (TGA) were performed upon drying of the as-prepared crystalline samples to remove solvent. As shown in Figure 3e, widely featureless TGA traces were observed up to the decomposition temperatures (T_d). For compound **2**, decomposition takes place between 320 and 400 °C, accompanied by a significant mass loss of 40.5% that accords with the release of all organic material including the silyl moiety. The differential scanning calorimetry (DSC) scans recorded in parallel provided detailed information about the melting range under glass formation and the decomposition at significantly higher temperatures. A broad endothermic feature observed for **2** in the temperature range of 167–188 °C (Figure 3f) is indicative for the first, while the exothermic feature centered around 358 °C, thus congruent with T_d, demonstrates the decomposition process. The corresponding data for **1** and **3** show endothermic glass formation at 212–231 °C for **1** and at 205–245 °C for **3**. Electron microscopy images confirm the physical transformation of the materials from microcrystalline solids (Figure 3g) to cluster-glass with smoother surfaces (Figure 3h–j). It is worth noting that the homogeneity of the resulting glass strongly depends on the heating time. Shorter heating time at the glass transition temperature leads to the formation of intermediate samples that exhibit small crystallites on the glass surface (Figure 3h,i), hence provide us with a means of controlling the transformation rate. The sample shown in Figure 3j shows high homogeneity of the surface after 30 min of exposing the crystalline material to T_g, hence indicating complete conversion of the crystalline material to a cluster-glass.

To explore whether that access to cluster-glass could be realized in an even simpler way and larger scale, 500 mg of the air-insensitive crystalline samples of **1** or **2** were placed on top of a glass slide (18 × 18 × 0.17 mm^3) or in a metal mold (Ø 3 mm). These were then transferred onto a heating plate and heated to their respective glass transition temperatures (T_g = 220 °C for **1** and T_g = 175 °C for **2**) for 30 min (glass slide) or 10 s (metal mold, Video S2, Supporting Information). The results of this treatment are illustrated in **Figure 4** for compound **2** as an example (Figure S38 for corresponding processing of compound **1**, Supporting Information). According to the PXRD diagram, the glass formation was successful and yielded an amorphous material (Figure 4a). As shown in Figure 4b, these cluster-glass materials exhibit the defined fracture surfaces typical for glass, and they are optically clearer as compared to those obtained in capillaries.

Again, the amorphization did not alter the chemical composition of the compounds, as verified by ^{1}H, ^{119}Sn, and ^{77}Se NMR spectroscopy of solutions of the glassy plates in $CDCl_3$, in which the material is readily soluble (Figure 4c), and by means of EDX analyses (Figure 4d). Scanning-electron microscopy (SEM) images recorded on the cluster-glass samples illustrate the very smooth surfaces and indicate the excellent air stability of these compounds that did not decompose during the heating process under air (Figure 4e–h). In summary, the experiment demonstrated an easy and inexpensive access to the cluster-glass materials at larger (gram) scale, which enables their potential use for applications in everyday life.

4. Quantum Chemical Investigations of the Inter-Cluster Interaction in the Amorphous Material

To understand the strikingly different material properties of these cluster compounds compared to their well-known homogeneous binary cousins, $[(PhC)_4(CH_2)_6]$, $[(PhSi)_4S_6]$, $[(PhSn)_4S_6]$, and $[(PhSn)_4Se_6]$, we performed quantum chemical studies on the single cluster and inter-cluster interactions for the compounds **1**–**3**. The structural parameters of the optimized single clusters show an increasing distortion from the smaller S-containing core structure of **1** to the largest Te-based core structure of **3**, which is consistent with the experimentally obtained structural parameters (Table S3 vs Table S2, Supporting Information).

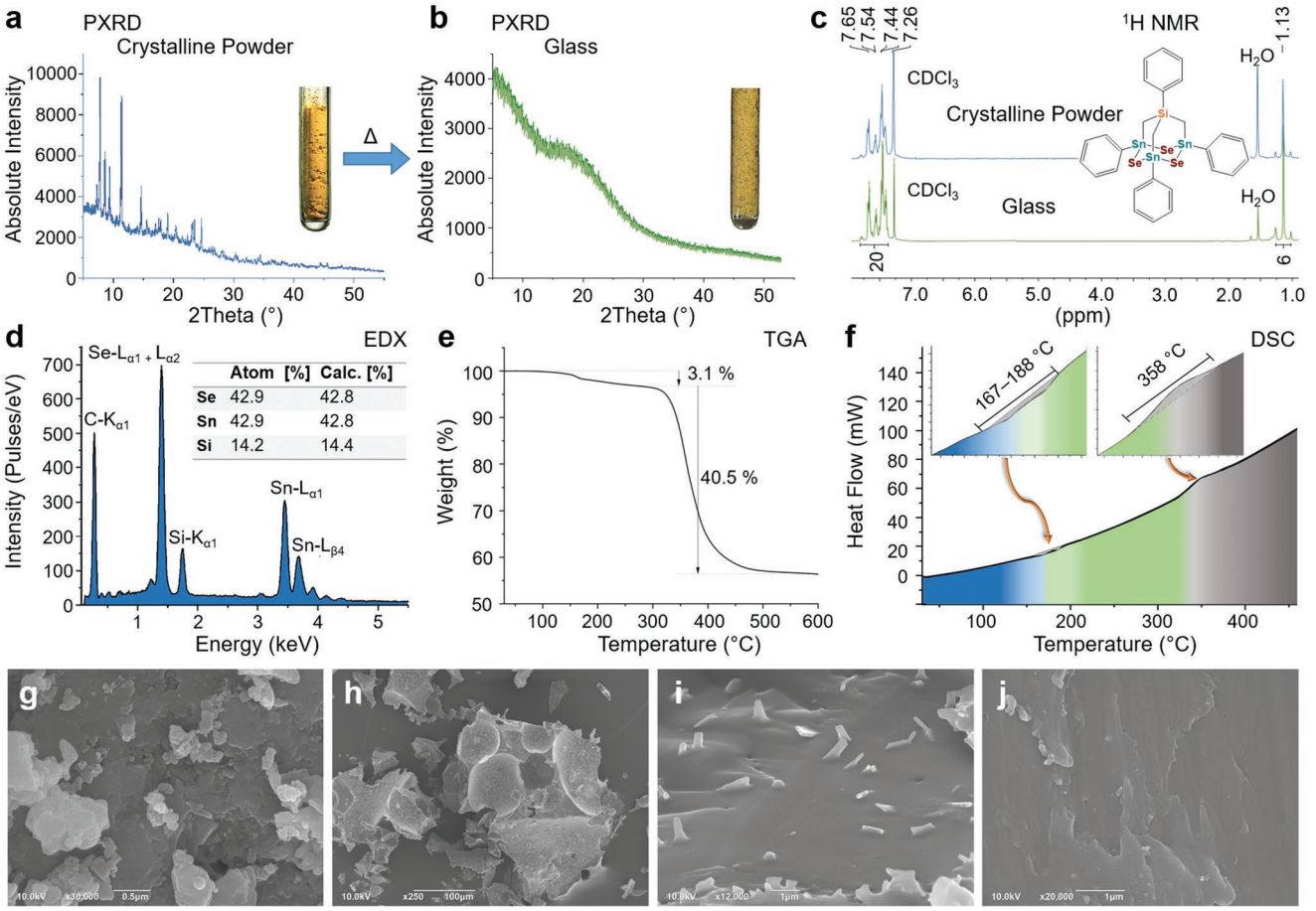

Figure 3. Properties of the cluster-glass formed by thermal treatment of quaternary adamantane-type cluster compounds. a) PXRD diagram and photograph of the crystalline material **2** (as an example for similarly behaving compounds **1**–**3**) after heating the material to the glass transition temperature T_g. b) PXRD diagram and photograph of the glass upon cooling down the capillary. c) ^{1}H NMR spectra of both samples dissolved in $CDCl_3$, proving their chemical identity. d) Energy-dispersive X-ray (EDX) spectrum confirming the Se:Sn:Si composition of the quaternary adamantane-type cluster compounds in the cluster-glass material. e) Thermal gravimetric analysis (TGA) curve indicating the decomposition temperature T_d around 350 °C. f) Differential scanning calorimetry (DSC) curve indicating the endothermic glass-formation step at the corresponding temperature of the glass transition (T_g) at 167–188 °C and the exothermic decomposition centering around 358 °C. g) Scanning electron microscopy (SEM) images of the as-prepared crystalline powder (×30 000). h–j) SEM images of the glassy surfaces after thermal treatment of the crystalline powder at T_g for 1 min (×250 and ×12 000) or for 30 min (×20 000).

The HOMOs of the three different cluster molecules are very similar to each other (Figure S40, Supporting Information). The main atomic orbital contributions to the HOMOs are located at the S, Se, or Te atoms in the cluster cores, respectively. The contributions to the LUMOs are distributed over the entire cluster for the S and Se compound, while for the telluride cluster, the Te atom contributions are dominant again. As expected, the natural charges (obtained from natural population analyses, NPA) of the Sn atoms decrease from 1.63 e in **1** to 1.25 e in **3**, which is in agreement with the negative charges of the chalcogen E atoms to develop from –0.76 to –0.39 e in the named direction. The influence of the chemical composition of the mixed cluster cores on the rotational barriers of the single substituents around themselves is negligible (<2 kJ mol^{-1}, thus below the thermal energy at room temperature; Table S4, Supporting Information), so we expect the molecules to behave similarly in regard of the possibility to form amorphous materials with randomly oriented organic substituents.

As a model system for understanding the intermolecular interactions in in the solids, we used cluster dimers, the structures of which were compared to the arrangement in the crystal structures. Both structural and energetic data were further compared to the values obtained for dimers of the homogenous clusters. Due to the nonuniformity of the core structures of the clusters, much more different relative orientations of two individuals are possible than for clusters with binary cores, which generally affects the properties of the dimer—as a minimal model for the interactions within the bulk material and the resulting properties. In order to account for this inhomogeneity, we created four different model dimers for each compound (**Figure 5**a), denominated as "Sn–Sn", "Sn–mix", "mix–mix (close)", and "mix–mix (opposite)", which differ in the relative positions of the Sn and Si atoms in the core structure. In all structures, an alternating orientation of the substituents was obtained as the most energetically favorable configuration.[26] More dimer

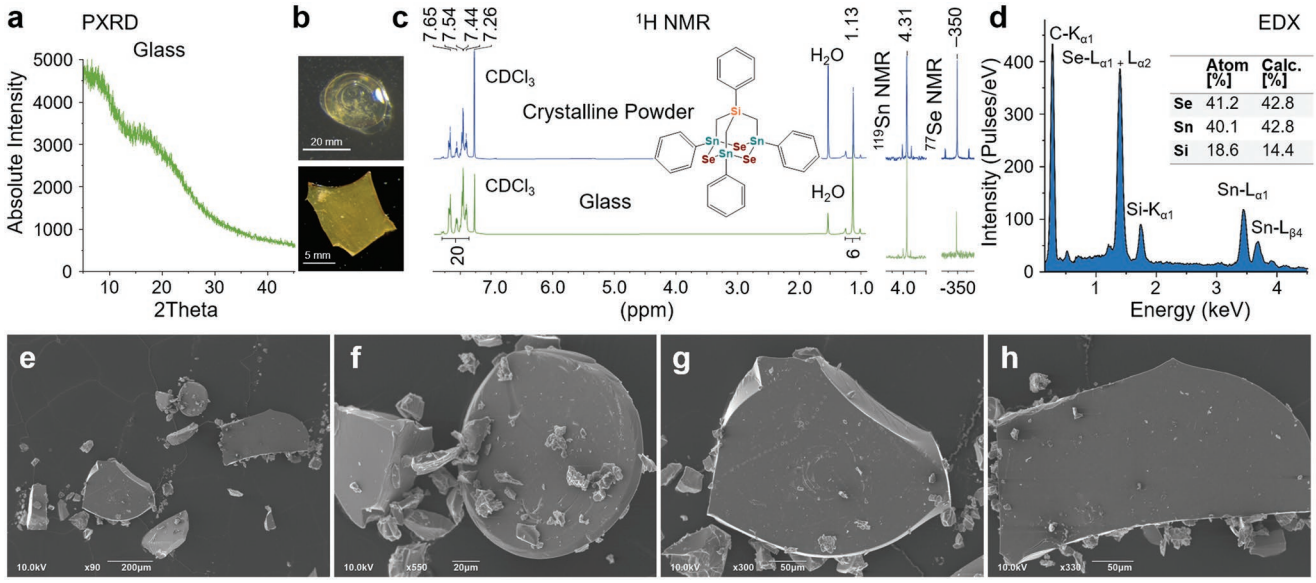

Figure 4. Cluster-glass formation by thermal treatment of quaternary adamantane-type cluster compounds on a heating plate. a) PXRD diagram of compound **2** (as an example for similarly behaving compounds **1** and **2**) after heating the crystalline material at T_g for 30 min. b) Light microscopy image of as-prepared platelets of the resulting cluster-glass. c) ^{1}H, ^{119}Sn, and ^{77}Se NMR spectra of the crystalline and the glassy samples dissolved in $CDCl_3$, proving their chemical identity. d) EDX spectrum confirming the Se:Sn:Si composition of the quaternary adamantane-type cluster compounds in the cluster-glass material. e–h) SEM images of close-ups in different magnifications of the cluster-glass samples of compound **2** (×90, ×550, ×300, and ×330) upon treatment of the crystalline powder samples on a heating plate at T_g for 30 min.

configurations are possible in theory, yet the given selection sufficiently represents the configurational space. Notably, the dimer structures are all quite similar in energy (see Figure S41, Supporting Information), which is in line with the finding that the crystalline material turns readily into an amorphous—hence, glassy—phase.

For the Se- and Te-based dimer structures, the energetically preferred structure is the "mix–mix (opposite)" dimer structure.

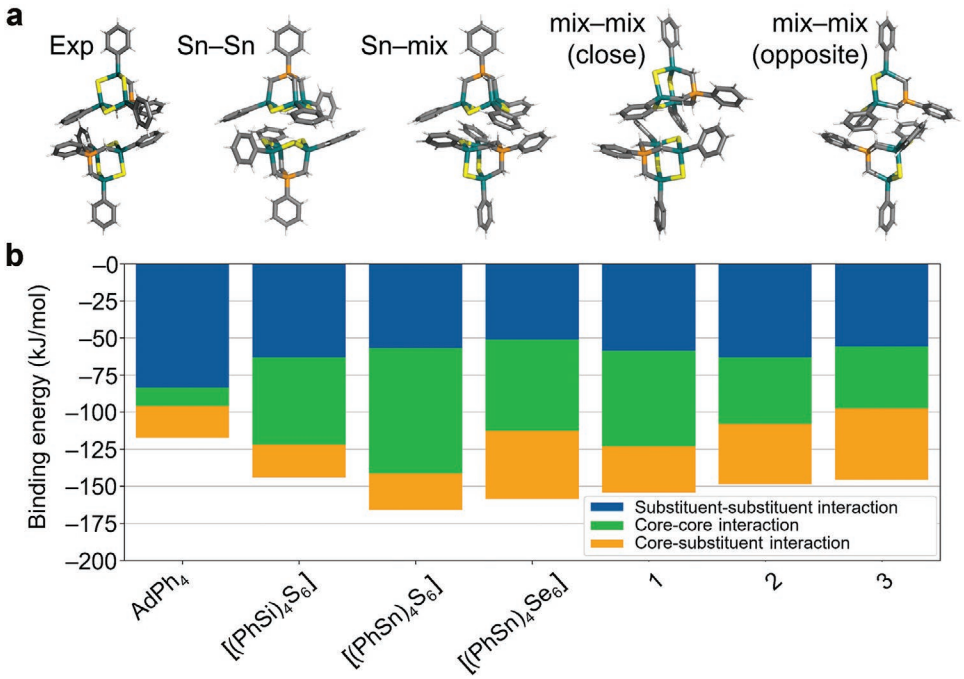

Figure 5. Different arrangements of the cluster dimer systems and decomposition of the binding energies. a) The figure shows a fragment of the crystals structures with the smallest core–core distance (Exp, **1**) and calculated dimer structures that were optimized at B3LYP-D4/cc-pVDZ(-PP) level of theory (see text). b) The graphic illustrates the energy decomposition values for the energetically preferred mixed-core dimer structures and the corresponding energetically preferred dimers of $AdPh_4$, $[(PhSi)_4S_6]$, $[(PhSn)_4S_6]$, and $[(PhSn)_4Se_6]$, calculated at B3LYP-D4/cc-pVDZ(-PP) level of theory.

The "mix–mix (close)" conformation provides higher overall relative energies due to increased steric hindrance of the substituents. For the S-containing structures, the "Sn–mix" structure is the energetically preferred one. The arrangement of the molecules within these cluster materials is influenced by the binding energy of the different structural parts (see Table S5, Supporting Information). The total binding energies of the mixed structures slightly decrease from **1** to **3**, which can be explained by the increasing core–core distance (6.818 Å for E = S, 7.021 Å for E = Se, and 7.246 for E = Te), and are a bit smaller than the total binding energies of the homogeneous clusters $[(PhSn)_4S_6]$ and $[(PhSn)_4Se_6]$. According to energy decomposition analyses (Figure 5b), the core–core interaction decreases from **1** to **3** due to the deformed structure of the mixed clusters, while the substituent–core interaction increases and the substituent–substituent interaction remains nearly constant. Thereby, the core–core interaction of **1** is lower than for the homogeneous cluster $[(PhSn)_4S_6]$, which is similar to a comparison of **2** with $[(PhSn)_4Se_6]$. In the same comparisons, it is noticeable that either both substituent–substituent and substituent–core interactions increase (S-based clusters) or the substituent–substituent interaction increases (Se-based clusters). The relative parts of the binding energies are summarized in Table S6 (Supporting Information).

The dimer with the smallest core–core distance of the experimental crystalline structure is very similar to the energetic minimum structures of the computed dimers of compounds **2** and **3** (Figure 5; and Figure S41, Supporting Information). In principle, this is also true for the energetically second most favorable structure of **1** (which is by only 5 kJ mol^{-1} higher in energy than the preferred structure). For the experimental and calculated structure, the same core configuration is present, with the crystalline structure slightly shifted, resulting in an increased core–core distance of 0.2–0.4 Å. Thus, the most stable optimized dimer is also found in the crystal structure. When considering other dimer structures extracted from the crystal structure, a strong influence of the surrounding clusters can be seen.

5. White-Light Generation due to Extreme Nonlinear Optical Properties of the Cluster-Glass

Optical spectroscopy was carried out on the crystalline powders of **1**–**3** and the cluster-glass materials obtained from them. For this, a thin layer of the crystalline powders and grains of glassy materials, respectively, were dispersed on a cover glass slip (**Figure 6**a). The cover glass was then placed in a sample chamber that was evacuated to at least 5×10^{-4} mbar. Consecutively, the sample chamber was placed in an experimental setup where the sample was illuminated by a continuous-wave (CW) laser diode operating at 980 nm. The light emitted by the sample was recorded in transmission geometry, while the sample was monitored via a simple confocal setup (Figure S42, Supporting Information).

For the crystalline powders, neither white-light nor second-harmonic generation is observed, as expected due to the centrosymmetric nature of the compounds' crystal structure. Above a certain laser-density threshold (≈1500 W cm^{-2}), however, the crystalline powders undergo a phase transition. Afterward, the material shows WLG at laser densities below the phase transition threshold. For grains of cluster-glass in contrast, a significantly lower threshold of ≈600 W cm^{-2} is required, as a consequence of the inherent intramolecular disorder in these amorphous materials.

The spectra resulting from white-light generation are shown in Figure 6b—along with those of $[(PhSn)_4S_6]$,[21] as reference. Excitation densities were 1100 W cm^{-2} for **1**, 1365 W cm^{-2} for **2**, 840 W cm^{-2} for **3**, and 322 W cm^{-2} for $[(PhSn)_4S_6]$, respectively. Like the reference compound, all three new compounds show broad-band emission that covers the whole wavelength range available by the experimental setup; as expected, **1** shows the closest similarity with the reference. To give a better understanding of the color impression of the generated white-light, the emitted spectrum is shown as it is perceived by the human eye under photopic vision (converted under use of the 1931 CIE photopic luminosity function, Figure S43, Supporting Information).[41] In this depiction, it becomes clear that the emitted spectrum covers the whole visible range and peaks at ≈600 nm (in radiometric representation, the emission of all samples rises monotonously toward the red part of the spectrum, see Figure S44, Supporting Information). Thus, the emitted light gives a warm-white color impression.

6. Quantum Chemical Investigations of the Nonlinear Optical Properties of Quaternary Adamantane-Type Cluster Compounds

Finally, the electronic and optical excitations of the compounds **1**, **2**, and **3** were investigated by means of occupation constrained as well as time-dependent density functional theory with a plane wave basis. The compounds are modeled as isolated molecules in their equilibrium geometry. The latter is in excellent agreement with measured values and with the quantum chemical calculations performed with a localized basis set.

Table 1 shows the key electronic properties of **1**, **2**, and **3**. Independent from the computational approach, the HOMO–LUMO gap gets smaller with increasing atomic number of the chalcogen atom, as expected, with increments of 0.4–0.6 eV when going from E = S to Se and to Te. The values calculated within density functional theory (DFT)-PBE (2.84–3.32 eV; Perdew–Burke–Ernzerhof (PBE) functional) are expected to underestimate the energy gap, while the quasiparticle energies yield a more realistic estimate (4.86–5.29 eV). Values calculated with hybrid-DFT methods (HSE06) are between DFT-PBE and quasiparticle gaps. The development of the HOMO–LUMO energy difference is mainly reflected in differences of atomic orbital contributions to the LUMOs of **1**–**3**, with increasing contributions of the cluster core atoms with increasing atomic number of E. Compound **3** bears the most significant differences in the contributions of the chalcogen p orbitals to both the HOMO and the LUMO in comparison to the lighter homologues. This is illustrated in Figure S45 (Supporting Information) by the orbitals calculated with DFT-PBE, which are in qualitative agreement with the orbitals shown in Figure S40

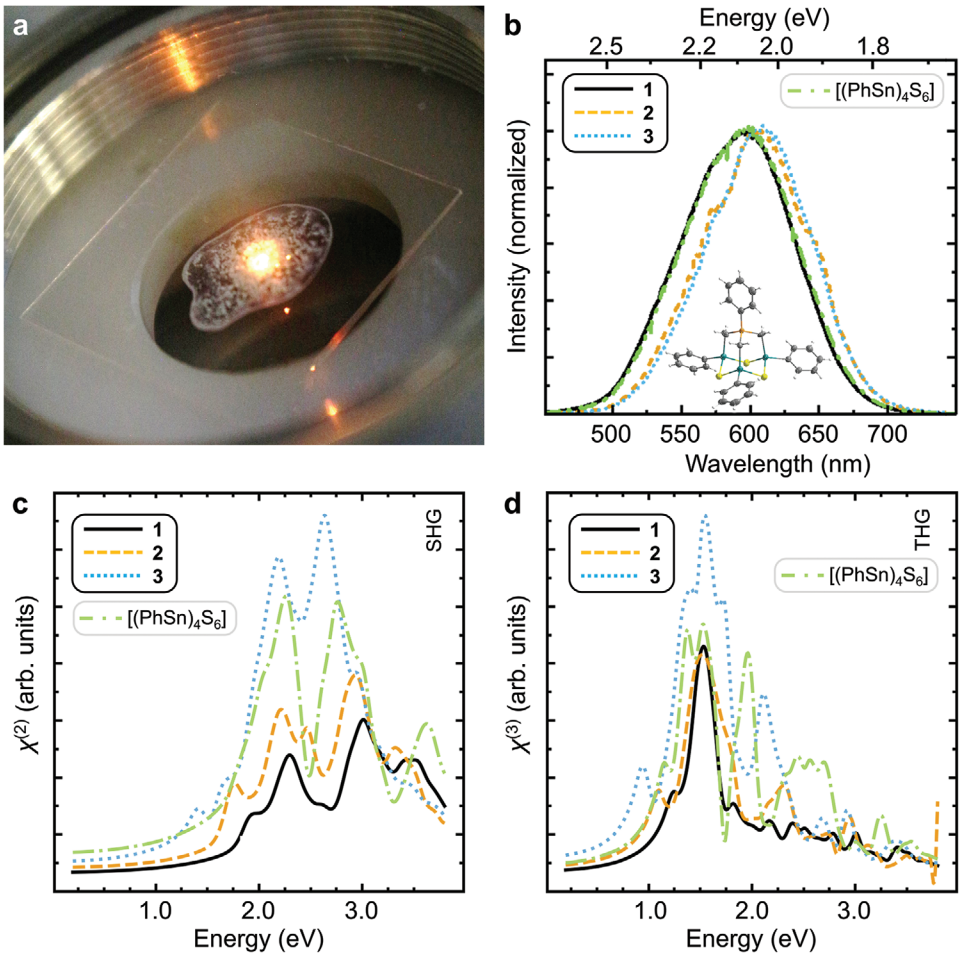

Figure 6. Emission characteristics and calculated SHG and THG spectra of compounds **1**–**3**. a) Photograph of Type I sample of **1** emitting white light upon excitation with a 980 nm continuous-wave laser. b) Emission spectrum following 980 nm excitation of Type I samples of **1** (black line), **2** (orange dashed), and **3** (blue dotted) with the emission of $[(PhSn)_4S_6]$ powder (green dashed–dotted) as reference.[21] To illustrate the color impression, the emission is plotted as photometric spectrum, i.e., as perceived under photopic vision (see main text for details). The molecular structure of **1** is given as a reminder in the inset. c) Averaged coefficients of the second-order polarizability tensor $\chi^{(2)}(\omega)$ calculated in the IPA within the time-domain approach for compounds **1** (black line), **2** (orange dashed), **3** (blue dotted), and $[(PhSn)_4S_6]$ (green dashed–dotted) as reference. d) Averaged coefficients of the $\chi^{(3)}$ tensor as calculated for compounds **1** (black line), **2** (orange dashed), **3** (blue dotted), and $[(PhSn)_4S_6]$ (green dashed–dotted) as reference, within the independent particle approximation in the time-domain approach.

(Supporting Information) obtained by application of DFT-B3LYP in a localized basis.

Table 1 also shows that the electron–hole excitation energies are within 0.1 eV of the HOMO–LUMO one-particle gap as calculated by DFT. This means that the electron–hole attraction nearly cancels out the quasiparticle effects and that optical excitation spectra calculated within the independent-particle approximation might be in good agreement with the experimental data. The similarity of electron–hole excitations estimated by different methods (E^{I}_{ex} and E_{ex}) further corroborates the validity of the approach.

Table 1. Electronic structure properties of compounds **1**–**3**. All quantities were calculated within DFT in the ΔSCF approximation and are given in eV.

	E_g^{PBE}	E_g^{HSE06}	E_g^{QP}	E_{ex}	E^{I}_{ex}
1	3.73	4.94	5.78	3.78	3.87
2	3.32	4.43	5.29	3.38	3.51
3	2.84	3.79	4.86	2.91	2.97

In order to compare the relative optical nonlinearity of the synthesized compounds, we have modeled the 2nd and 3rd order hyperpolarizabilities, $\chi^{(2)}$ and $\chi^{(3)}$, corresponding to the second-harmonic generation (SHG) and third harmonic generation (THG) coefficients for the isolated clusters. The calculated coefficients are averaged over different tensor components and shown in Figure 6c,d, respectively, along with those calculated newly for $[(PhSn)_4S_6]$ as reference.

Isolated molecules of all three compounds are noncentrosymmetric (although corresponding crystals are) and display nonvanishing SHG coefficients. The magnitude of $\chi^{(2)}$ is comparable to that of strong SHG emitters such as the XPh_4 (X = Si, Ge, Sn, and Pb) tetra-phenyls recently investigated.[42] The 2nd order nonlinear optical response of **1**, **2**, and **3** seems to correlate with the structural asymmetry in the cluster core. The

cluster with the largest core distortion (compound **3**) indeed features a 2nd order optical susceptibility which is roughly twice as large as that of compounds **1** and **2** (Figure 6c). Moreover, due to the limited spatial overlap of HOMO and LUMO in **1** and **2**, direct HOMO–LUMO transitions have a reduced probability. Thus, the onset of the optical absorption is larger than the HOMO–LUMO gap, and the first peak in SHG occurs at about 1.8 eV, slightly above half the DFT calculated electronic gap. Concerning **3** instead, the first SHG peak occurs exactly at half HOMO–LUMO gap, as expected for two-photon processes.

The THG coefficients shown in Figure 6d suggest important third-order optical response for all compounds. Similar to the case of SHG, **3** has the most intense nonlinear response, with the first peak related to three photon processes occurring at one third of the DFT calculated HOMO–LUMO electronic gap. We observe that all the calculated coefficients feature high peaks and low deeps at which the nonlinearities are almost quenched, i.e., they strongly depend on the energy of the incoming photons. Thus, the optical answer of the glassy materials is also expected to depend on the exciting wavelength.

In order to identify possible modifications of the optical response of the isolated molecules upon crystallization, the nonlinear optical coefficients of compound **1** in its crystalline form have been calculated. SHG and THG spectra are shown in Figures S46 and S47 (Supporting Information), respectively. The close similarity to the spectra of the parent molecule suggests that the optical nonlinearity is an intrinsic property of the molecules and does not arise from intermolecular interactions.

The computational studies of the optical response of **1**, **2**, and **3** from first principles, thus show that **1** and **2** have a very similar electronic structure, while **3** shows a higher core asymmetry and a somewhat different LUMO form, resulting in a smaller electronic bandgap. All compounds in their molecular form are characterized by 2nd and 3rd order nonlinear optical response, which is required in the different physical processes leading to WLG.[33] In particular, **3** shows the highest nonlinear optical coefficients both for SHG as well as for THG. However, the similar magnitude of the white light emission measured for **1**, **2**, and **3** suggests that WLG is a process which is both related to the compound habitus and to the intrinsic optical response of the parent clusters.

7. Conclusion and Outlook

With the aim of overcoming the problem of limited processability of materials suitable for low-cost white-light generation based on amorphous molecular materials, we developed a new class of robust glassy materials that are readily fabricated by mild heating of crystalline powders of inorganic–organic hybrid cluster compounds of the general type $[(PhSi)(CH_2)_3(PhSn)E_3]$ (E = S, Se, Te) based on quaternary adamantane-type cluster cores. The materials are denoted as "cluster-glass", in accordance with the observed glass transition process and with their transparent and homogeneous appearance. By reverting the cluster-glass formation by dissolving the material and recrystallization of the compounds from such solutions, as well as by solution spectroscopy, it was proven that the clusters remain full intact in the glassy material.

As desired, the glassy materials show excellent white-light emission properties upon irradiation by a continuous-wave infrared laser diode. In addition, under slightly elevated temperatures, the robust glassy solids can be adopted to any shape required for technical devices. Theoretical studies corroborate the importance of the quaternary nature of the cluster cores for the observed structural and optical phenomena.

On the basis of our findings, we can we can affirm that the white-light generation process requires the delocalized electron density of the substituents and not an extended core, that an asymmetric core, however, can reduce the overall system symmetry thus relaxing the selection rules involved in the electronic transitions, and enhancing the optical nonlinearities.

With this study, we put the research in the field of innovative and inexpensive high-brilliance white-light emitters to the next level by provision of a new type of controllably and reversibly amorphizable cluster compounds that form well-processable, robust cluster-glass materials.

8. Experimental Section

General Preparative Methods: All solvents were dried by standard methods. Trichloro(phenyl)silane, bromochloromethane, triphenyltin chloride, iodine, hydrogen chloride (gas), potassium hydroxide, and *n*-butyllithium, sodium, were commercially available.

Starting from $PhSiCl_3$ the silicon atom is first functionalized in excellent yields with $-CH_2Cl$ groups to form $PhSi(CH_2Cl)_3$, followed by introduction of the $SnPh_3$ group to produce $PhSi(CH_2SnPh_3)_3$. The selective conversion of Sn—Ph into Sn—Cl in $PhSi(CH_2SnPhCl_2)_3$ can be quantitatively achieved without rupture of the $Sn-CH_2$ or $Si-CH_2$ bond, if the $-CH_2-$ group is bound to −SiR. In addition, the $-SiCH_2-$ moiety increases the product solubility in organic solvents, thus facilitating the purification process.

Synthesis and Characterization of Tris(chloromethyl)(phenyl)silane, $PhSi(CH_2Cl)_3$: A solution of $PhSiCl_3$ (7.0 g, 31.0 mmol) in dry THF (400 mL) and $BrCH_2Cl$ (12.0 g, 93.0 mmol) under argon atmosphere were cooled to –78 °C, whereupon 39.7 mL (93.0 mmol) of a 2.5 M solution of *n*-butyl lithium in hexane/THF (200 mL) at the same temperature were added during 1 h (the *n*-butyl lithium solution was added via a special horizontally-elongated side neck of the three-necked flask, which itself was immersed in the cooling bath to ensure precooling of the *n*-butyl lithium solution before getting into contact with the reaction mixture). The solution was warmed to room temperature and stirred overnight, then hydrolyzed and the product extracted with dichloromethane. After removal of the solvent, the residue was redissolved in hexane and purified by column chromatography using hexane as eluent. Subsequent removal of the solvent in vacuo yielded 3.54 g (45%) of $PhSi(CH_2Cl)_3$; $^{29}Si\{^1H\}$ NMR (79.5 MHz, $CDCl_3$, 298 K, δ): –8.63; ^1H NMR (400.2 MHz, $CDCl_3$, 298 K, δ): 3.35 (s, 6H, $SiCH_2$), 7.49–7.74 (m, 5H, $C_{12}H_8$); $^{13}C\{^1H\}$ NMR (100.6 MHz, $CDCl_3$, 298 K, δ): 24.6 ($SiCH_2$), 134.1 (C1), 134.7 (C2), 128.5 (C3), 131.4 (C4).

Synthesis and Characterization of Phenyl[(triphenylstannyl)methyl]silane, $PhSi(CH_2SnPh_3)_3$: A solution of Ph_3SnCl (11.4 g, 29.7 mmol) in dry THF (400 mL), sodium (0.68 g, 29.7 mmol) and catalytic amount of naphthalene were placed under argon atmosphere into a 500 mL three-necked flask equipped with a magnetic stirring bar. The reaction mixture was stirred for 3 days, after that the reaction mixture was filtered whereupon the solution was cooled to –78 °C followed by dropwise addition of a solution of $PhSi(CH_2Cl)_3$ (2.5 g, 9.9 mmol) in 50 mL of THF. After stirred overnight, the solvent was distilled off and the residue redissolved in 200 mL of CH_2Cl_2. Then, the reaction mixture was hydrolyzed and the organic layer extracted with CH_2Cl_2, dried over $MgSO_4$ and filtered. After removal of the solvent, the residue was washed with hexane (3 × 25 mL) and dried in vacuo to yield 2.3 g

(5.9 mmol, 20%) of $PhSi(CH_2SnPh_3)_3$; $^{119}Sn\{^1H\}$ NMR (186.5 MHz, $CDCl_3$, 300 K, δ): –90.7; $^{29}Si\{^1H\}$ NMR (99.4 MHz, $CDCl_3$, 300 K, δ): 3.22; ^1H NMR (300.1 MHz, $CDCl_3$, 300 K, δ): 0.51 (s, 6H, $SiCH_2$), 6.86–7.31 (m, 50H, $H_{aromatic}$); $^{13}C\{^1H\}$ NMR (75.5 MHz, $CDCl_3$, 300 K, δ): –2.6 ($SiCH_2$), 140.0 (C1'), 134.3 (C2'), 127.7 (C3'), 128,1 (C4'), 128.8 [$^4J(^{13}C—^{117/119}Sn)$ = 11 Hz, C_p], 128.4 [$^3J(^{13}C—^{117/119}Sn)$ = 50 Hz, C_m], 137.1 [$^2J(^{13}C—^{117/119}Sn)$ = 37 Hz, C_o], 139.6 (C_i); IR: ν = 443 (s), 483 (w), 569 (m), 631 (m), 694 (s), 723 (s), 767 (w), 853 (w), 908 (w), 997 (m), 1073 (m), 1114 (w), 1157 (w), 1188 (w), 1299 (w), 1332 (w), 1358 (w), 1426 (m), 1480 (w), 1578 (w), 1639 (w), 1759 (w), 1813 (w), 1875 (w), 2874 (w), 2916 (w), 2952 (w), 2987 (w), 3012 (w), 3046 (w), 3132 cm^{-1} (w); MS (ESI^-) *m/z*: $[M+Cl]^-$ calcd. for $C_{63}H_{56}ClSiSn_3$, 1233.0925; found, 1233.0924. Anal. calcd. for $C_{63}H_{56}SiSn_3$: C 63.2, H 4.7; found: C 63.0, H 4.8.

Synthesis and Characterization of Tris{[dichloro(phenyl)stannyl]methyl}(phenyl)silane, $PhSi(CH_2SnPhCl_2)_3$: 3.0 g of precursor $PhSi(CH_2SnPh_3)_3$ (2.50 mmol) and 50 mL of dichloromethane were placed into a 100 mL ball flask equipped with a magnetic stirring bar. The solution was cooled to 0 °C, whereupon 2 M of HCl in ether (7.5 mL, 15.0 mmol) was added drop by drop during 60 min. The reaction mixture was allowed to stir overnight. Subsequently, the solvent was evaporated and the byproduct (benzene) removed under vacuum to give $PhSi(CH_2SnPhCl_2)_3$ as a viscous brown compound in 95% yield (2.25 g, 2.38 mmol). $^{119}Sn\{^1H\}$ NMR (186.5 MHz, $CDCl_3$, 300 K, δ): 39.9; $^{29}Si\{^1H\}$ NMR (99.4 MHz, $CDCl_3$, 300 K, δ): –0.59; ^1H NMR (300.1 MHz, $CDCl_3$, 300 K, δ): 1.68 (s, 6H, $SiCH_2$), 7.33–7.58 (m, 20H, $H_{aromatic}$); $^{13}C\{^1H\}$ NMR (75.5 MHz, $CDCl_3$, 300 K, δ): 10.7 ($SiCH_2$), 138.8 (C1'), 133.9 (C2'), 129.0 (C3'), 131.7 (C4'), 131.7 (C_p), 129.6 (C_m), 134.5 (C_o), 139.0 (C_i); IR: ν = 440 (s), 506 (w), 581 (m), 645 (s), 690 (s), 721 (s), 760 (w), 850 (w), 915 (w), 996 (w), 1020 (m), 1108 (m), 1160 (w), 1191 (w), 1262 (w), 1302 (w), 1333 (w), 1354 (w), 1431 (m), 1480 (w), 1577 (w), 1589 (w), 1645 (w), 1763 (w), 1881 (w), 1901 (w), 1958 (w), 2996 (w), 2953 (w), 3050 (w), 3067 cm^{-1} (w); Anal. calcd. for $C_{27}H_{26}Cl_6SiSn_3$: C 34.2, H 2.8; found: C 33.7, H 2.7.

Synthesis and Characterization of 1,3,5,7-Tetraphenyl-2,4,9-trithia-7-sila-1,3,5-tristanna-adamantane, $PhSi(CH_2SnPhS)_3$ (1): To a solution of $PhSi(CH_2SnPhCl_2)_3$ (1.0 g, 1.1 mmol) in 20 mL of dry toluene were added 0.57 g (3.3 mmol) of TMS_2S and the reaction mixture was stirred at room temperature 24 h. After the solvent was removed in vacuo, the solid was washed 3 times with dry hexane and filtered. The product is obtained in 60% yield (0.53 g, 0.66 mmol). m.p.: 215–220 °C. $^{119}Sn\{^1H\}$ NMR (186.5 MHz, $CDCl_3$, 300 K, δ): 100.7; $^{29}Si\{^1H\}$ NMR (99.4 MHz, $CDCl_3$, 300 K,δ): 4.69; ^1H NMR (500.2 MHz, $CDCl_3$, 300 K, δ): 1.07 (s, 6H, $SiCH_2$), 7.49–7.74 (m, 20H, $H_{aromatic}$); $^{13}C\{^1H\}$ NMR (125.8 MHz, $CDCl_3$, 300 K, δ): 4.1 ($SiCH_2$), 141.9 (C1'), 132.3 (C2'), 128.2 (C3'), 129.6 (C4'), 130.4 [$^4J(^{13}C—^{117/119}Sn)$ = 15.8 Hz, C_p], 129.1 [$^3J(^{13}C—^{117/119}Sn)$ = 73.7 Hz, C_m], 134.5 [$^2J(^{13}C—^{117/119}Sn)$ = 56.7 Hz, C_o], 141.9 (C_i); IR: ν = 445 (s), 538 (s), 656 (s), 694 (s), 728 (s), 755 (s), 973 (m), 996 (m), 1071 (m), 1104 (m), 1189 (w), 1261 (w), 1300 (w), 1331 (w), 1429 (m), 1479 (w), 1576 (w), 1771 (w), 1816 (w), 1884 (w), 1960 (w), 2886 (w), 2941 (w), 3015 (w), 3042 (w), 3063 cm^{-1} (w); MS (ESI^-) *m/z*: $[M+Cl]^-$ calcd. for $C_{27}H_{26}ClS_3SiSn_3$, 864.7709; found, 864.7743. Anal. calcd. for $C_{27}H_{26}S_3SiSn_3$: C 39.0, H 3.2, S 11.5; found: C 37.8, H 3.4, 11.1.

Synthesis and Characterization of 1,3,5,7-Tetraphenyl-2,4,9-triselena-7-sila-1,3,5-tristanna-adamantane, $PhSi(CH_2SnPhSe)_3$ (2): To a solution of $PhSi(CH_2SnPhCl_2)_3$ (1.0 g, 1.1 mmol) in 20 mL of dry toluene were added 0.71 g (3.3 mmol) of TMS_2Se and the reaction mixture was stirred at room temperature 24 h. After the solvent was removed in vacuo, the solid was washed 3 times with dry hexane and filtered. The product is obtained in 63% yield (0.64 g, 0.69 mmol). m.p.: 174–180 °C. $^{119}Sn\{^1H\}$ NMR (186.5 MHz, $CDCl_3$, 300 K, δ): 5.0; $^{29}Si\{^1H\}$ NMR (99.4 MHz, $CDCl_3$, 300 K, δ): 5.0; $^{77}Se\{^1H\}$ NMR (95.4 MHz, $CDCl_3$, 300 K, δ): –349; ^1H NMR (500.2 MHz, $CDCl_3$, 300 K, δ): 1.14 (s, 6H, $SiCH_2$), 7.40–7.67 (m, 20H, $H_{aromatic}$); $^{13}C\{^1H\}$ NMR (125.8 MHz, $CDCl_3$, 300 K, δ): 4.0 ($SiCH_2$), 142.8 (C1'), 132.2 (C2'), 128.2 (C3'), 129.5 (C4'), 130.3 [$^4J(^{13}C—^{117/119}Sn)$ = 16.4 Hz, C_p], 129.1 [$^3J(^{13}C—^{117/119}Sn)$ = 69.7 Hz, C_m], 134.4 [$^2J(^{13}C—^{117/119}Sn)$ = 56.2 Hz, C_o], 140.6 (C_i); IR: ν = 441 (s), 534 (s), 655 (s), 691 (s), 707 (s), 725 (s), 756 (s), 846 (w), 909 (w), 975 (m), 1014 (m), 1070 (m), 1103 (m), 1188 (w), 1260 (w), 1297 (w), 1330 (w), 1341 (w), 1428 (m), 1477 (w), 1575 (w), 1635 (w), 1808 (w), 1870 (w), 1890 (w), 2876 (w), 2927 (w), 2937 (w), 2988 (w), 3008 (w), 3037 (w), 3059 (w), 3133 cm^{-1} (w); MS (ESI^-) *m/z*: $[M+Cl]^-$ calcd. for $C_{27}H_{26}ClSe_3SiSn_3$, 1006.6071; found, 1006.6140. Anal. calcd. for $C_{27}H_{26}Se_3SiSn_3$: C 33.3, H 2.70; found: C 32.0, H 2.69.

Synthesis and Characterization of 1,3,5,7-Tetraphenyl-2,4,9-tritellura-7-sila-1,3,5-tristanna-adamantane, $PhSi(CH_2SnPhTe)_3$ (3): To a solution of $PhSi(CH_2SnPhCl_2)_3$ (1.0 g, 1.1 mmol) in 20 mL of dry toluene were added 0.87 g (3.3 mmol) of TMS_2Te and the reaction mixture was stirred at room temperature 24 h. After the solvent was removed in vacuo, and the solid was washed 3 times with dry hexane and filtered. The product is obtained in 80% yield (4.1 g, 4.5 mmol). m.p.: 205–210 °C. $^{119}Sn\{^1H\}$ NMR (111.9 MHz, $CDCl_3$, 300 K, δ): –246 [$^1J(^{125}Te—^{117/119}Sn)$ = 2543 Hz]; $^{29}Si\{^1H\}$ NMR (59.6 MHz, $CDCl_3$, 300 K, δ): 5.5; $^{125}Te\{^1H\}$ NMR (157.8 MHz, $CDCl_3$, 300 K, δ): –862 [$^1J(^{117/119}Sn—^{125}Te)$ = 3071/2934 Hz]; ^1H NMR (500.1 MHz, $CDCl_3$, 300 K, δ): 1.37 (s, 6H, $SiCH_2$), 7.37–7.65 (m, 20H, $H_{romatic}$); $^{13}C\{^1H\}$ NMR (125.8 MHz, $CDCl_3$, 300 K, δ): 2.79 ($SiCH_2$), 144.4 (C1'), 132.0 (C2'), 128.2 (C3'), 129.4 (C4'), 130.1 [$^4J(^{13}C—^{117/119}Sn)$ = 14.1 Hz, C_p], 128.9 [$^3J(^{13}C—^{117/119}Sn)$ = 61.5 Hz, C_m], 134.9 [$^2J(^{13}C—^{117/119}Sn)$ = 53.0 Hz, C_o], 137.4 [$^1J(^{13}C—^{117/119}Sn)$ = 453/474 Hz, C_i]; IR: ν = 441 (s), 524 (s), 641 (s), 693 (s), 724 (s), 753 (s), 842 (m), 966 (m), 1006 (m), 1066 (m), 1101 (m), 1155 (m), 1187 (w), 1249 (w), 1296 (w), 1328 (w), 1337 (w), 1425 (m), 1476 (w), 1635 (w), 1809 (w), 1872 (w), 1946 (w), 2872 (w), 2921 (w), 2955 (w), 3004 (w), 3036 (w), 3058 cm^{-1} (w); MS (ESI^-) *m/z*: $[M+Cl]^-$ calcd. for $C_{27}H_{26}ClTe_3SiSn_3$, 1154.5713; found, 1154.5721. Anal. calcd. for $C_{27}H_{26}Te_3SiSn_3$: C 29.0, H 2.4; found: C 29.6, H 2.6.

Glass Formation of 1,3,5,7-Tetraphenyl-2,4,9-trithia-7-sila-1,3,5-tristanna-adamantane, $PhSi(CH_2SnPhS)_3$ (Capillary): A sample of 5 mg of crystalline compound **1** was placed in a capillary for determining the melting point (80 × 1.3 mm). The capillary was left under vacuum for 30 min and was sealed thereupon. It was heated in a melting point measuring equipment for 30 min until reaching the glass transition temperature (T_g = 209–233 °C), with a temperature ramp of 1 °C s^{-1}. Subsequently, it was removed from the melting point measuring equipment and allowed to cool down to room temperature. The glass that formed was collected and analyzed by different optical and spectroscopic techniques. PXRD served to confirm a change of the material to an amorphous solid. By means of EDX spectroscopy, the composition of the glass was confirmed to be identical with that of the crystalline material. ^1H NMR was used to confirm that the chemical identity of the sample was not changed, with the same signals being observed for both the crystalline and the glassy materials in solution. Images were obtained by SEM, which indicates smooth surfaces of the glassy material in contrast to the observations made for the crystalline material. Additional images were taken under a microscope for visual inspection. The process and the results are illustrated in Figure S37 (Supporting Information).

Glass Formation of 1,3,5,7-Tetraphenyl-2,4,9-trithia-7-sila-1,3,5-tristanna-adamantane, $PhSi(CH_2SnPhS)_3$ (Flat Glass): A sample of 500 mg of crystalline compound **1** was placed on a glass slide (18 × 18 mm, 0.17 mm) on top of a heating plate. It was heated up during 30 min to the temperature T_g (209–233 °C) for 30 min, and subsequently allowed to cool down to room temperature, which afforded the glass. Alternatively, 500 mg of the sample are placed in a metallic mold and heated on the heating place within a few seconds. The amorphousness of the material was confirmed by PXRD. The elemental composition of the glass is identical to that of the crystalline material and to that of the glass obtained within a capillary, as confirmed by EDX analyses. ^1H, ^{119}Sn, and ^{77}Se NMR carried out on solutions of the glassy material indicated identical chemical shits as solutions of the crystalline compound. The surface of the millimeter-sized glassy materials was inspected by means of light microscopy and SEM, indicating flat surfaces. The process and the results are illustrated in Figure S38 (Supporting Information).

Glass Formation of 1,3,5,7-Tetraphenyl-2,4,9-triselena-7-sila-1,3,5-tristanna-adamantane, $PhSi(CH_2SnPhSe)_3$(Capillary): A sample of 5 mg of crystalline compound **2** was placed in a capillary for determining the melting point (80 × 1.3 mm). The capillary was left under vacuum for 30 min and was sealed thereupon. It was heated in a melting point measuring equipment for 30 min until reaching the glass transition temperature (T_g = 167–188 °C), with a temperature ramp of 1 °C s^{-1}. Subsequently, it was removed from the melting point measuring

equipment and allowed to cool down to room temperature. The glass that formed was collected and analyzed by different optical and spectroscopic techniques. PXRD served to confirm a change of the material to an amorphous solid. By means of EDX spectroscopy, the composition of the glass was confirmed to be identical with that of the crystalline material. ^{1}H NMR was used to confirm that the chemical identity of the sample was not changed, with the same signals being observed for both the crystalline and the glassy materials in solution. Images were obtained by SEM, which indicates smooth surfaces of the glassy material in contrast to the observations made for the crystalline material. Additional images were taken under a microscope for visual inspection. The process and the results are illustrated in the main document.

Glass Formation of 1,3,5,7-Tetraphenyl-2,4,9-triselena-7-sila-1,3,5-tristanna-adamantane, $PhSi(CH_2SnPhSe)_3$ (Flat Glass): A sample of 500 mg of crystalline compound **1** was placed on a glass slide (18 × 18 mm, 0.17 mm) on top of a heating plate. It was heated up during 30 min to the temperature T_g (167–188 °C) for 30 min, and subsequently allowed to cool down to room temperature, which afforded the glass. Alternatively, 500 mg of the sample are placed in a metallic mold and heated on the heating place within a few seconds. The amorphousness of the material was confirmed by PXRD. The elemental composition of the glass is identical to that of the crystalline material and to that of the glass obtained within a capillary, as confirmed by EDX analyses. ^{1}H, ^{119}Sn, and ^{77}Se NMR carried out on solutions of the glassy material indicated identical chemical shits as solutions of the crystalline compound. The surface of the millimeter-sized glassy materials was inspected by means of light microscopy and SEM, indicating flat surfaces. The process and the results are illustrated in the main document.

Glass Formation of 1,3,5,7-Tetraphenyl-2,4,9-tritellura-7-sila-1,3,5-tristanna-adamantane, $PhSi(CH_2SnPhTe)_3$ (Capillary): A sample of 5 mg of crystalline compound **3** was placed in a capillary for determining the melting point (80 × 1.3 mm). The capillary was left under vacuum for 30 min and was sealed thereupon. It was heated in a melting point measuring equipment for 30 min until reaching the glass transition temperature (T_g = 205–243 °C), with a temperature ramp of 1 °C s^{-1}. Subsequently, it was removed from the melting point measuring equipment and allowed to cool down to room temperature. The glass that formed was collected and analyzed by different optical and spectroscopic techniques. PXRD served to confirm a change of the material to an amorphous solid. By means of EDX spectroscopy, the composition of the glass was confirmed to be identical with that of the crystalline material. ^{1}H NMR was used to confirm that the chemical identity of the sample was not changed, with the same signals being observed for both the crystalline and the glassy materials in solution. Images were obtained by SEM, which indicates smooth surfaces of the glassy material in contrast to the observations made for the crystalline material. Images were also taken under a microscope for visual inspection. The process and the results are illustrated in Figure S39 (Supporting Information).

Glass Formation of 1,3,5,7-Tetraphenyl-2,4,9-tritellura-7-sila-1,3,5-tristanna-adamantane, $PhSi(CH_2SnPhTe)_3$ (Flat Glass): For the formation of type II glasses of the tellurium compound **3**, attempts were made both under air and under argon atmosphere. Under air, the process leads to decomposition owing to the higher air sensitivity of **3**, in contrast to the respective properties of compounds **1** and **2**. A second challenge for this compound (and not for **1** and **2**) is the close proximity of the melting range and the decomposition temperature (see Figure S39, Supporting Information). So, even under inert conditions, the formation of type II glasses on a heating plate was not achieved, as the decomposition point is so close to the melting point that the only rough temperature control of the heating plate did not allow for stopping at exactly the right temperature. This problem does not apply to the melting point meter, in which the temperature can be tuned very finely.

Crystalline and Glass Materials Analysis: Elemental analyses of H, C, and S were carried out on a CHN(S)-Analyzer vario MICRO CUBE using samples dried under high vacuum for 15 h. The melting points were determined in a sealed glass tube on a Krüss KSP1N melting-point apparatus. The IR spectra were recorded on a Bruker Tensor 37 spectrometer with ATR unit. 1D (^{1}H, ^{13}C, ^{29}Si, ^{119}Sn) and 2D (COSY, HSQC) nuclear magnetic resonance (NMR) studies were recorded at room temperature on Bruker DRX 300 and DRX 500 spectrometers. Standard internal and external references were used: tetramethylsilane (δ^{1}H = 0, δ^{13}C = 0, and δ^{29}Si = 0) and tetramethyltin (δ^{29}Sn = 0). Electrospray-ionization (ESI) mass spectra and high-resolution (HR) ESI mass spectra were recorded on an LTQ-FT Ultramass spectrometer (Thermo Fischer Scientific) with $CHCl_3$/MeCN as the mobile phase. EDX spectroscopy was performed using the EDX detector XFlash 5010 of Bruker Nano GmbH coupled with the scanning electron microscope Jeol JIB-4610F. For SEM, a Jeol JIB-4601F microscope was employed. PXRD studies were carried out on a Stoe STADI MP X-ray powder diffractometer. The data for the X-ray structural analyses were collected at 100(2) K with Mo-Kα radiation (λ = 0.7107 Å) on an imaging plate detector system Stoe IPDS II using X-AREA v1.88. The structures were solved by ShelXT15.[43] The refinement was done by full-matrix-least-squares methods against F^2 with the program ShelXL using Olex^2 v1.3.0 software. Structure solution and refinement data are summarized in Table S1 (Supporting Information), selected structural parameters are listed in Table S2 (Supporting Information). The TGA/DSC measurements were performed simultaneously on a METTLER TOLEDO with a heating rate of 10 K min^{-1} in N_2 atmosphere in an Al_2O_3 crucible. The compounds decomposes slowly above 593–673 K in an exothermic process. The decomposition is also observable optically by the generation of a black powder. The mass loss is presumably dominated by organic fragments. Images are provided in Figure S37 (Supporting Information) for compound **1**, the main document for compound **2**, and in Figure S39 (Supporting Information) for compound **3**.

Light Microscopy: Visual inspection of the glassy products was done with a stereo light microscope SteREO Discovery.V8 by Carl Zeiss. The microscope was equipped with a high-intensive cold-light source CL 1500 ECO, an Achromat S 0.63x objective (FWD 107 mm), a PL 10x/21 Br ocular, and an AxioCam MRc 5 camera with a 60N-C 2/3'' 0,63x adapter. The raw photo material was examined by the AxioVision40 × 64 4.9.1 SP1 software. Images are provided in Figure S38 (Supporting Information) for compound **1** and in the main document for compound **2**.

Methods of the Quantum Chemical Calculations (Localized Basis): The energetically preferred monomer cluster structure was created by utilizing the iterative meta-dynamics with genetic structure crossing (iMTD-GC) algorithm and then optimized using the GFN2-xTB algorithm.[44,45] The results were then reoptimized using DFT. The dimer model systems were then manually created from these optimized monomer structures in different relative orientations and optimized using DFT.

All optimizations and single point calculations were performed at DFT level of theory using the Turbomole software package version 7.5.[46,47] Structural optimizations as well as single point calculations were carried out using the hybrid functional B3LYP[48–52] with an m3 grid[53] size and resolution-of-identity (RI) approximation,[54] an electronic convergence criteria of 10^{-7} Ha and a convergence maximum norm of cartesian gradient of 10^{-4} Ha. Subsequent frequency calculations have shown no imaginary frequencies, so the observed structures can be considered to be minimum structures. Test calculations with an m4 grid size and without RI approximation for $[(MeSi)_4S_6]$ show a negligible difference in energy (0.1% for m3/m4 and 0.2% for non-RI/RI). Medium- and long-range dispersion interactions were accounted for using the D4 dispersion correction by Grimme et al.[55,56] A correlation-consistent Dunning-type basis set (cc-pVDZ) was used for all elements except for Sn and Te,[57,58] where an energy-consistent scalar-relativistic effective core potential ECP28MDF was employed in combination with the corresponding basis set cc-pVDZ-PP.[58–60] Test calculations using the cc-pVTZ basis set resulted in an binding energy difference of only <12% for $[(PhSn)_4S_6]$. A selection of calculated bond lengths are provided in Table S3 (Supporting Information), rotation barriers of the dimers are given in Table S4 (Supporting Information), and the total binding energies of the dimers are listed in Tables S5 and S6 (Supporting Information). Plots of the frontier molecular orbitals are illustrated in Figure S40 (Supporting

Information) and relative energies of the different dimer configurations are summarized in Figure S41 (Supporting Information).

The binding energies were calculated for the optimized dimer structures, where the monomers were extracted and calculated via a single point calculations without performing additional structural optimizations of the monomers. In this way, the binding energies are calculated and not the dissociation energies, where the structures of the monomers are optimized. In contrast to the dissociation energy, the binding energy does not include the deformation energy for dimer formation. The binding energy was calculated using the following formula

$$E_{\mathrm{BE}} = E_{\mathrm{dimer(Opt)}} - E_{\mathrm{monomer1(SP)}} - E_{\mathrm{monomer2(SP)}} \quad (1)$$

The binding energy decomposition was performed by separating different parts of the system from the optimized dimer. To calculate the core–core and substituent–substituent interactions, the broken bonds were saturated with hydrogen atoms. Then, single point calculations were performed for the saturated, separated structures of the dimers and the differences were calculated to determine the binding energies of the different structural parts. The core–substituent binding energies were calculated from the difference of the cluster–cluster binding energy and the sum of the core–core and substituent–substituent binding energies.

Experimental Setup of the Spectroscopic Measurements: To investigate the response of the samples under infrared irradiation, an in-house build confocal setup (see Figure S42, Supporting Information) is used. The emission of a fiber coupled continuous-wave laser diode is collimated, relayed via a dielectric mirror (Thorlabs FESH0900) and then focused onto the sample. Spot size of the laser is ≈100 µm in diameter.

At the same time, the focusing lens is used to image the sample onto a standard CCD camera (Bresser MirkoCamII) where in this beam path the dielectric mirror is used as a shortpass filter. To additionally block residual laser light from the CCD camera, a bandpass filter (Schott KG3) is placed in the beam path.

The light emitted by the sample is collected in transmission geometry and imaged onto the entrance slit of a compact spectrometer (Avantes AvaSpec-2048L-USB2). Also, in this beam path, a bandpass filter (Schott KG3) is used to block residual laser light. To account for the absorption of the filter and the response function of the spectrometer, the whole system is calibrated using a halogen calibrated light source (Ocean Optics – HL-3).The obtained correction is used to report the radiometric spectrum.

Optical Absorption Spectra: The spectra were recorded on a standard UV–vis machine (Perkin Elmer Lambda 1050) equipped with the integrating sphere detection module (Labsphere). Transmission was measured by placing the sample at the entrance port of the integrating sphere. Afterward the sample was mounted on the backside of the integrating sphere to determine the reflection spectrum from the sample's surface. Absorption (A) is then calculated from transmission (T) and reflection (R) via: $A = 1 - T - R$.

Calculation of Photometric Spectra: To give a better representation of the color impression of the emitted white light, the measured spectra are converted to photometric spectra using the standard photopic luminosity function.[41] For this, the measured values are corrected for the system response. The photopic luminosity function (see Figure S43, Supporting Information) is interpolated to match the measured wavelength values. Then the measured values are multiplied by the photopic luminosity function.

Radiometric representation of the broad-band emission of compounds **1**–**3** are shown in Figure S44 (Supporting Information) for comparison.

Methods of the Quantum Chemical Calculations (Plane Waves Basis): The Vienna ab initio simulation package[61,62] and Quantum Espresso[63,64] are employed to evaluate the structural, electronic, and optical properties of **1**, **2**, and **3** (as isolated molecules or in their crystalline phase) by periodic DFT. Isolated molecules are modeled within a box of 25 × 25 × 25 Å. Projected augmented wave pseudopotentials[65,66] are used to describe the ion–electron interaction. The generalized gradient approximation[50] in the PBE formulation[67,68] is used to describe the electronic many-body interactions. The atomic positions are relaxed until the residual Hellmann–Feynman forces[69] are lower than 0.001 eV Å^{-1}. The accurate modeling of the long-range van der Waals (vdW) interactions is a major challenge for DFT with (semi)local exchange-correlation (XC) functionals. Different ab initio as well as semiempirical corrections schemes are tested to tackle this challenge. The results presented in this paper are obtained with a semiempirical DFT-D3 scheme with zero damping,[70,71] which is sufficiently accurate to allow for valid conclusions concerning structural properties. Plane waves up to a cutoff of 610 eV (VASP) and 55 Ry (QE) are used as basis for the expansion of electron wave functions. The crystalline phases are modeled within the primitive unit cells containing four formula units. A Monkhorst-Pack 4 × 3 × 4 k-points mesh[72] for the energy integration of the Brillouin zone ensures numerical convergence.

While DFT calculations of the electronic ground state considerably underestimate the electronic excitations, reliable values for quasiparticle gaps and exciton energies are obtained in a very efficient way within the ΔSCF method.[73,74] Within this approximation, quasiparticle gaps are given by the difference

$$E^{\mathrm{QP}} = E(N+1,\vec{R}) + E(N-1,\vec{R}) - 2E(N,\vec{R}) \quad (2)$$

where $\vec{R}$ represents the equilibrium geometry and N is the number of electrons in a neutral system. This difference can be interpreted as the difference between ionization energy and electron affinity. As the quantities in Equation (2) are computed using charged cells, interactions between periodic images affect the calculations. However, the E^{QP} depend linearly on $1/L$, where L is the cell side. The corrected values shown in this work is obtained using cells of different size and extrapolating to $L \to \infty$.

The lowest excitonic excitation, represented by a hole h in the HOMO and an electron e in the LUMO, is estimated by

$$E_{\mathrm{ex}} = E(e-h,\vec{R}) - E(N,\vec{R}) \quad (3)$$

whereby $E(e-h,\vec{R})$ is the energy of the system with an electron–hole pair at the groundstate equilibrium geometry $\vec{R}$. The situation in which one electron occupies the LUMO leaving a hole in the HOMO can be also estimated via Janak's theorem[75,76] as the difference of the energy eigenvalues of half occupied HOMO and LUMO electronic levels

$$E_{\mathrm{ex}}^{\mathrm{J}} = \varepsilon^{\mathrm{LUMO}}(0.5) - \varepsilon^{\mathrm{HOMO}}(0.5) \quad (4)$$

Illustrations of the frontier molecular orbitals are provided in Figure S45 (Supporting Information).

Hyperpolarizabilities of in principle any order (in the case $\chi^{(2)}$ and $\chi^{(3)}$) are calculated in the time-domain by developing the dynamical polarization in a power series of the applied field[77,78]

$$P_\alpha = \sum_\beta \chi^{(1)}_{\alpha\beta} E_\beta + \sum_{\beta,\gamma} \chi^{(2)}_{\alpha\beta\gamma} E_\beta E_\gamma + \sum_{\beta,\gamma,\delta} \chi^{(3)}_{\alpha\beta\gamma\delta} E_\beta E_\gamma E_\delta + \cdots \quad (5)$$

where $\chi^{(n)}$ is the nth order frequency dependent susceptibility and E_β is the cartesian component in β direction of the electric field. The dynamical polarization is calculated within the Berry-phase formulation.[79] The nonlinear optical coefficients of isolated molecules are obtained by averaging the components of the corresponding tensor. Second and third order optical susceptibility are plotted in Figures S46 and S47 (Supporting Information).

Supporting Information

Supporting Information is available from the Wiley Online Library or from the author.

Acknowledgements

This work was supported by the Deutsche Forschungsgemeinschaft within the framework or the Research Unit FOR 2824. I.R.L. acknowledges support by SECTEI (Secretaría de Educación Ciencia, Tecnología e Innovación de la Ciudad de México) and the Alexander von Humboldt Foundation. Calculations for this research were conducted on the Lichtenberg high performance computer of the TU Darmstadt and at the Höchstleistungrechenzentrum Stuttgart (HLRS). The authors furthermore acknowledge the computational resources provided by the HPC Core Facility and the HRZ of the Justus-Liebig-Universität Gießen.

Open access funding enabled and organized by Projekt DEAL.

Conflict of Interest

The authors declare no conflict of interest.

Author Contributions

I.R.L. and J.C. conceived and performed the synthetic experiments, collected single-crystal X-ray crystallographic data, solved and refined the structures, performed NMR and Infrared spectroscopy, ESI mass spectrometry, and prepared samples for glass formation and further analyses (PXRD, TGA/DSC analysis, EDX and SEM). N.W.R. performed the white-light measurements. S.Sch. and F.Z. performed the theoretical studies. S.D., S.S., D.M., and N.W.R. supervised the work. All authors co-wrote the paper.

Data Availability Statement

The data that support the findings of this study regarding X-ray diffraction studies and quantum chemical calculations are available in the supplementary material of this article. All other raw data are available from the corresponding author upon reasonable request.

Keywords

amorphous molecular materials, cluster-glass, extreme nonlinear optical properties, optical spectroscopy, white-light generation

Received: April 13, 2022
Revised: June 4, 2022
Published online:

[1] J. Wu, G. Zheng, X. Liu, J. Qiu, *Chem. Soc. Rev.* **2020**, *49*, 3461.
[2] N. W. Rosemann, J. P. Eußner, A. Beyer, S. W. Koch, K. Volz, S. Dehnen, S. Chatterjee, *Science* **2016**, *352*, 1301.
[3] P. Osewski, A. Belardini, E. Petronijevic, M. Centini, G. Leahu, R. Diduszko, D. A. Pawlak, C. Sibilia, *Sci. Rep.* **2017**, *7*, 45247.
[4] J. Gotta, T. B. Shalom, S. Aslanoglou, A. Cifuentes-Rius, N. H. Voelcker, R. Elnathan, O. Shoseyov, S. Richter, *Adv. Funct. Mater.* **2018**, *28*, 1706967.
[5] H. Su, Y. Chen, K. Wong, *Adv. Funct. Mater.* **2020**, *30*, 1906898.
[6] X. Lu, G. Moille, A. Rao, D. A. Westly, K. Srinivasan, *Nat. Photonics* **2021**, *15*, 131.
[7] J. Zhao, A. Fieramosca, R. Bao, W. Du, K. Dini, R. Su, J. Feng, Y. Luo, D. Sanvitto, T. C. H. Liew, Q. Xiong, *Nat. Nanotechnol.* **2022**, *17*, 396.
[8] D. A. Akimov, M. Schmitt, R. Maksimenka, K. V. Dukel'skii, Y. N. Kondrat'ev, A. V. Khokhlov, V. S. Shevandin, W. Kiefer, A. M. Zheltikov, *Appl. Phys. B* **2003**, *77*, 299.
[9] M. Guignard, V. Nazabal, J. Troles, F. Smektala, H. Zeghlache, Y. Quiquempois, A. Kudlinski, G. Martinelli, *Opt. Express* **2005**, *13*, 789.
[10] R. R. Alfano (Ed.), Springer, New York **2006**.
[11] J. He, M. Zeller, A. D. Hunter, Z. Xu, *J. Am. Chem. Soc.* **2012**, *134*, 1553.
[12] W.-H. Lai, A. S. Haynes, L. Frazer, Y.-M. Chang, T.-K. Liu, J.-F. Lin, I.-C. Liang, H.-S. Sheu, J. B. Ketterson, M. G. Kanatzidis, K.-F. Hsu, *Chem. Mater.* **2015**, *27*, 1316.
[13] G. Li, Q. Liu, K. Wu, Z. Yang, S. Pan, *Dalton Trans.* **2017**, *46*, 2778.
[14] S. Nakamura, T. Mukai, M. Senoh, *Appl. Phys. Lett.* **1994**, *64*, 1687.
[15] S. Nakamura, *Rev. Mod. Phys.* **2015**, *87*, 1139.
[16] C. Poriel, J. Rault-Berthelot, *Adv. Funct. Mater.* **2020**, *30*, 1910040.
[17] J. E. Beetar, M. Nrisimhamurty, T.-C. Truong, G. C. Nagar, Y. Liu, J. Nesper, O. Suarez, F. Rivas, Y. Wu, B. Shim, M. Chini, *Sci. Adv.* **2020**, *6*, eabb5375.
[18] F. Meng, C. Lapre, C. Billet, T. Sylvestre, J.-M. Merolla, C. Finot, S. K. Turitsyn, G. Genty, J. M. Dudley, *Nat. Commun.* **2021**, *12*, 5567.
[19] R. Fan, Y.-Y. Lin, L. Chang, A. Boes, J. Bowers, J.-W. Liu, C.-H. Lin, T.-K. Wang, J. Qiao, H.-C. Kuo, G.-R. Lin, M.-H. Shih, Y.-J. Hung, Y.-J. Chiu, C.-K. Lee, *Sci. Rep.* **2021**, *11*, 7978.
[20] H. Xiang, R. Wang, J. Chen, F. Li, H. Zeng, *Light: Sci. Appl.* **2021**, *10*, 206.
[21] N. W. Rosemann, J. P. Eußner, E. Dornsiepen, S. Chatterjee, S. Dehnen, *J. Am. Chem. Soc.* **2016**, *138*, 16224.
[22] N. W. Rosemann, H. Locke, P. R. Schreiner, S. Chatterjee, *Adv. Opt. Mater.* **2018**, *6*, 1701162.
[23] B. D. Klee, E. Dornsiepen, J. R. Stellhorn, B. Paulus, S. Hosokawa, S. Dehnen, W.-C. Pilgrim, *Phys. Status Solidi B* **2018**, *255*, 1800083.
[24] E. Dornsiepen, F. Dobener, N. Mengel, O. Lenchuk, C. Dues, S. Sanna, D. Mollenhauer, S. Chatterjee, S. Dehnen, *Adv. Opt. Mater.* **2019**, *7*, 1801793.
[25] E. Dornsiepen, F. Dobener, S. Chatterjee, S. Dehnen, *Angew. Chem., Int. Ed.* **2019**, *58*, 17041.
[26] K. Hanau, S. Schwan, M. R. Schäfer, M. J. Müller, C. Dues, N. Rinn, S. Sanna, S. Chatterjee, D. Mollenhauer, S. Dehnen, *Angew. Chem., Int. Ed.* **2021**, *60*, 1176.
[27] D. Troegel, F. Möller, C. Burschka, R. Tacke, *Organometallics* **2009**, *28*, 5765.
[28] K. Merzweiler, H. Kraus, *Z. Naturforsch. B* **1994**, *49*, 621.
[29] K. Schwedtmann, A. Hepp, K. Schwedtmann, J. J. Weigand, F. Lips, *Eur. J. Inorg. Chem.* **2019**, *2*, 4719.
[30] I. Rojas-León, H. Alnasr, K. Jurkschat, M. G. Vasquez-Ríos, I. F. Hernández-Ahuactzi, H. Höpfl, *Chem. – Eur. J.* **2018**, *24*, 4547.
[31] D. Dakternieks, K. Jurkschat, H. Wu, E. R. T. Tiekink, *Organometallics* **1993**, *12*, 2788.
[32] H. Lange, U. Herzog, U. Böhme, G. Rheinwald, *J. Organomet. Chem.* **2002**, *660*, 43.
[33] C. H. W. Jones, R. D. Sharma, S. P. Taneja, *Can. J. Chem.* **1986**, *64*, 980.
[34] M. Bouška, L. Dostál, F. De Proft, A. Růžička, A. Lyčka, R. Jambor, *Chem. – Eur. J.* **2011**, *17*, 455.
[35] J. P. Eußner, R. O. Kusche, S. Dehnen, *Chem. – Eur. J.* **2015**, *21*, 12376.
[36] U. Herzog, G. Rheinwald, *J. Organomet. Chem.* **2001**, *628*, 133.
[37] T. Kunz, O. Şahin, C. Schrenk, A. Schnepf, *Dalton Trans.* **2021**, *50*, 2663.
[38] E. Dornsiepen, S. Dehnen, *Dalton Trans.* **2019**, *48*, 3671.
[39] S. Heimann, M. Hołyńska, S. Dehnen, *Chem. Commun.* **2011**, *47*, 1881.
[40] J. Ayari, C. R. Göb, I. M. Oppel, M. Lutter, W. Hiller, K. Jurkschat, *Angew. Chem., Int. Ed.* **2020**, *59*, 23892.

[41] CIE C., in Commission Internationale de l'eclairage Proceedings, 1931, Cambridge University Press, Cambridge, UK **1932**.
[42] K. Eberheim, C. Dues, C. Attaccalite, M. J. Müller, S. Schwan, D. Mollenhauer, S. Chatterjee, S. Sanna, *J. Phys. Chem. C* **2022**, *126*, 3713.
[43] G. M. Sheldrick, *Acta Crystallogr., Sect. A: Found. Adv.* **2015**, *71*, 3.
[44] S. Grimme, *J. Chem. Theory Comput.* **2019**, *15*, 2847.
[45] P. Pracht, F. Bohle, S. Grimme, *Phys. Chem. Chem. Phys.* **2020**, *22*, 7169.
[46] S. G. Balasubramani, G. P. Chen, S. Coriani, M. Diedenhofen, M. S. Frank, Y. J. Franzke, F. Furche, R. Grotjahn, M. E. Harding, C. Hättig, A. Hellweg, B. Helmich-Paris, C. Holzer, U. Huniar, M. Kaupp, A. Marefat Khah, S. Karbalaei Khani, T. Müller, F. Mack, B. D. Nguyen, S. M. Parker, E. Perlt, D. Rappoport, K. Reiter, S. Roy, M. Rückert, G. Schmitz, M. Sierka, E. Tapavicza, D. P. Tew, et al., *J. Chem. Phys.* **2020**, *152*, 184107.
[47] TURBOMOLE V7.5 2020, A Development of University of Karlsruhe and Forschungszentrum Karlsruhe GmbH, 1989–2007, TURBOMOLE GmbH, since 2007. https://www.turbomole.org (accessed: April 2022).
[48] P. A. M. Dirac, *Math. Proc. Cambridge Philos. Soc.* **1930**, *26*, 376.
[49] J. C. Slater, *Phys. Rev.* **1951**, *81*, 385.
[50] J. P. Perdew, J. A. Chevary, S. H. Vosko, K. A. Jackson, M. R. Pederson, D. J. Singh, C. Fiolhais, *Phys. Rev. B* **1992**, *46*, 6671.
[51] K. Reiter, F. Mack, F. Weigend, *J. Chem. Theory Comput.* **2018**, *14*, 191.
[52] A. D. Becke, *Phys. Rev. A* **1988**, *38*, 3098.
[53] K. Eichkorn, F. Weigend, O. Treutler, R. Ahlrichs, *Theor. Chem. Acta* **1997**, *97*, 119.
[54] K. Eichkorn, O. Treutler, H. Öhm, M. Häser, R. Ahlrichs, *Chem. Phys. Lett.* **1995**, *242*, 652.
[55] E. Caldeweyher, C. Bannwarth, S. Grimme, *J. Chem. Phys.* **2017**, *147*, 034112.
[56] E. Caldeweyher, S. Ehlert, A. Hansen, H. Neugebauer, S. Spicher, C. Bannwarth, S. Grimme, *J. Chem. Phys.* **2019**, *150*, 154122.
[57] T. H. Dunning, *J. Chem. Phys.* **1989**, *90*, 1007.
[58] K. L. Schuchardt, B. T. Didier, T. Elsethagen, L. Sun, V. Gurumoorthi, J. Chase, J. Li, T. L. Windus, *J. Chem. Inf. Model.* **2007**, *47*, 1045.
[59] K. A. Peterson, D. Figgen, E. Goll, H. Stoll, M. Dolg, *J. Chem. Phys.* **2003**, *119*, 11113.
[60] B. P. Pritchard, D. Altarawy, B. Didier, T. D. Gibson, T. L. Windus, *J. Chem. Inf. Model.* **2019**, *59*, 4814.
[61] G. Kresse, J. Furthmüller, *Comput. Mater. Sci.* **1996**, *6*, 15.
[62] G. Kresse, J. Furthmüller, *Phys. Rev. B* **1996**, *54*, 11169.
[63] P. Giannozzi, O. Andreussi, T. Brumme, O. Bunau, M. Buongiorno Nardelli, M. Calandra, R. Car, C. Cavazzoni, D. Ceresoli, M. Cococcioni, N. Colonna, I. Carnimeo, A. Dal Corso, S. de Gironcoli, P. Delugas, R. A. DiStasio, A. Ferretti, A. Floris, G. Fratesi, G. Fugallo, R. Gebauer, U. Gerstmann, F. Giustino, T. Gorni, J. Jia, M. Kawamura, H.-Y. Ko, A. Kokalj, E. Küçükbenli, M. Lazzeri, et al., *J. Phys. Condens. Matter* **2017**, *29*, 465901.
[64] P. Giannozzi, S. Baroni, N. Bonini, M. Calandra, R. Car, C. Cavazzoni, D. Ceresoli, G. L. Chiarotti, M. Cococcioni, I. Dabo, A. Dal Corso, S. de Gironcoli, S. Fabris, G. Fratesi, R. Gebauer, U. Gerstmann, C. Gougoussis, A. Kokalj, M. Lazzeri, L. Martin-Samos, N. Marzari, F. Mauri, R. Mazzarello, S. Paolini, A. Pasquarello, L. Paulatto, C. Sbraccia, S. Scandolo, G. Sclauzero, A. P. Seitsonen, et al., *J. Phys. Condens. Matter* **2009**, *21*, 395502.
[65] G. Kresse, D. Joubert, *Phys. Rev. B* **1999**, *59*, 1758.
[66] P. E. Blöchl, *Phys. Rev. B* **1994**, *50*, 17953.
[67] J. P. Perdew, K. Burke, M. Ernzerhof, *Phys. Rev. Lett.* **1996**, *77*, 3865.
[68] J. P. Perdew, K. Burke, M. Ernzerhof, *Phys. Rev. Lett.* **1997**, *78*, 1396.
[69] R. P. Feynman, *Phys. Rev.* **1939**, *56*, 340.
[70] S. Grimme, *J. Comput. Chem.* **2006**, *27*, 1787.
[71] S. Grimme, J. Antony, S. Ehrlich, H. Krieg, *J. Chem. Phys.* **2010**, *132*, 154104.
[72] H. J. Monkhorst, J. D. Pack, *Phys. Rev. B* **1976**, *13*, 5188.
[73] H.-C. Weissker, J. Furthmüller, F. Bechstedt, *Phys. Rev. B* **2004**, *69*, 115310.
[74] A. Riefer, E. Rauls, W. G. Schmidt, J. Eberhard, I. Stoll, J. Mattay, *Phys. Rev. B* **2012**, *85*, 165202.
[75] S. Sanna, T. Frauenheim, U. Gerstmann, *Phys. Rev. B* **2008**, *78*, 085201.
[76] J. F. Janak, *Phys. Rev. B* **1978**, *18*, 7165.
[77] C. Attaccalite, M. Grüning, A. Marini, *Phys. Rev. B* **2011**, *84*, 245110.
[78] C. Attaccalite, M. Grüning, *Phys. Rev. B* **2013**, *88*, 235113.
[79] I. Souza, J. Íñiguez, D. Vanderbilt, *Phys. Rev. B* **2004**, *69*, 085106.